Quantum-Well Infrared Photodetector Structure Synthesis: Methodology and Experimental Verification

Neena Imam, Elias N. Glytsis, *Senior Member, IEEE*, Thomas K. Gaylord, *Fellow, IEEE*, Kwong-Kit Choi, *Senior Member, IEEE*, Peter G. Newman, and Lisa Detter-Hoskin

***Abstract*—A numerical method for global optimization of quantum-well infrared photodetector (QWIP) performance parameters is presented and experimentally verified. The single-band effective-mass Schroedinger equation is solved by employing the argument principle method (APM) to extract both the bound and quasibound eigen-energies of the quantum heterostructure. APM is combined with a simulated annealing algorithm to determine a set of device design parameters such as potential barrier height V_i, layer thickness d_i, number of material layers N, total device length, applied bias $V_{\rm Bias}$ etc., for which the QWIP performance is within a predetermined convergence criterion. The method presented incorporates the effect of energy-dependent effective mass of electrons in nonparabolic conduction bands. The present model can handle many optimization parameters and can incorporate fabrication constraints to achieve physically realizable devices. In addition, the method is not limited to the optimization of absorption structures, and can be used for other instersubband devices such as electron-wave Fabry–Perot filters and quantum-cascade lasers. The strength and versatility of the present method are demonstrated by the design of a bicolor equal-absorption-peak QWIP structure, and experimental verification of the zero-bias absorption spectrum is presented.**

***Index Terms*—Intersubband, mid-infrared, optimization, photodetector, quantum heterostructure, quasibound states, simulated annealing.**

I. Motivation

INTERSUBBAND transitions involving two or more energy eigenstates are now commonly used for infrared detection of energies lower than the bandgap energies of semiconductors. Quantum-well infrared photodetectors (QWIPs), based on mature GaAs–AlGaAs technology, provide higher fabrication uniformity and better production yield compared to alternative HgCdTe detector technology [1]. In addition, the design of GaAs–$Al_xGa_{1-x}As$ based QWIPs can be tailored for diverse applications due to manipulable aluminum compositions and layer thicknesses. Infrared photodetectors with a single quantum well have been studied in detail [2], [3]. The optical, electronic and transport properties of these basic QWIP structures are well understood [4]. Detectors for a free-space wavelength of 10 μm with low dark current and high detectivity at 77 K have been demonstrated that meet the requirements of focal plane array applications [5]. Recently, a large format and high uniformity GaAs–AlGaAs QWIP focal plane array (FPA) camera has been reported [6]. Despite the impressive progress in both theoretical and experimental aspects of QWIP research, there is still a need for a systematic synthesis methodology that can perform global optimization over all QWIP performance variables. The optimization of QWIPs is a complex and often involved process. Many performance parameters such as the transition energy ΔE_{ij} (between states i and j), peak wavelength λ_P, dipole matrix element Z_{ij}, absorption coefficient α_{ji}, etc. have to be evaluated. The relationship between these parameters and the corresponding tradeoffs may become very complex in QWIPs exploiting multiple electronic subbands. One example is the bound-to-extended state transition QWIP. The performance of these QWIPs is very sensitive to the position of the upper state. If the upper state resides too close to the top of the potential barrier, large thermionic currents degrade detector performance [7]. Placing it too high will broaden the spectral width [8]. Therefore, careful consideration must be given to the optimum placement of the upper energy state. The optimization of all the performance parameters can become counter-intuitive particularly if the number of parameters is large.

As is evident from the above discussion, an optimization technique that weighs all the performance variables of QWIPs appropriately, and determines the device structure accordingly is highly desirable. The global optimization of QWIP structures is a relatively new area. To our knowledge, the methodology presented in this paper is the only global optimization technique reported to date for the design of QWIPs. This is a global optimization technique in the sense that an objective function is formulated as a function of the M parameters of interest and the optimization algorithm is globally convergent in the M parameter space. The objective functions are flexible and can incorporate fabrication constraints. The method presented incorporates an efficient tool for determination of the eigenstates of the structure and is versatile for symmetric/asymmetric, biased/unbiased devices. In addition, this method is capable of including the effect of conduction band nonparabolicity. The present method is applied to the optimized synthesis of a bicolor equal-absorption-peak QWIP structure.

Manuscript received September 10, 2002; revised November 13, 2002. This research was supported by the State of Georgia Yamacraw Mission and by the National Science Foundation under Grant ERC-94–02723

N. Imam, E. N. Glytsis, and T. K. Gaylord are with the School of Electrical and Computer Engineering and Microelectronics Research Center, Georgia Institute of Technology, Atlanta, GA 30332 USA.

K.-K. Choi and P. G. Newman are with the U.S. Army Research Laboratory, Adelphi, MD 20783 USA.

L. Detter-Hoskin is with the Georgia Tech Research Institute, Atlanta, GA 30332 USA.

Digital Object Identifier 10.1109/JQE.2002.808162

Employing bandgap engineering, it is possible to extend the functionality of a GaAs–$Al_xGa_{1-x}As$ based QWIP to perform multicolor detection using various quantum well designs. Multispectral applications may be very useful in the spectral analysis of infrared sources and target discrimination. Subsequently, considerable research effort has been focused on developing multicolor QWIPs for detection in the 3–5-μm mid-wavelength (MWIR) and 8–12-μm long-wavelength (LWIR) atmospheric transmission windows. In conventional single-wavelength QWIPs, the same well and barrier structure is repeated many times. In one possible configuration of multicolor QWIPs, several conventional QWIP structures with different wavelength selectivities are stacked together [9]. Various colors are accessed by changing the applied bias. One disadvantage of this configuration is the extremely thick structures. Also, each detector must be contacted individually. Another approach is to use different transitions within the same well/barrier structure. Symmetric [10] and asymmetric [11], [12] quantum wells have been utilized for this purpose. Other QWIP configurations have been studied including coupled quantum wells with graded barriers, and triple-well structures [13]. Dual-band QWIPs that manipulate Γ–X conduction-band coupling in indirect gap materials have also been reported [14]. None of the above-mentioned configurations exhibits equal absorption peaks at the detection wavelengths (λ_P). While there have been a number of different schemes proposed for multicolor detection, no work has been reported on deliberately and systematically equalizing the absorption peaks. Multiband QWIPs can have equal absorption peaks, yielding uniform performance over the photon-energy (wavelength) range of interest, by optimizing the fundamental parameters of the heterostructure.

In the following sections, the design and optimization of a bicolor QWIP structure with equal-absorption peaks at two distinct and well-resolved detection wavelengths are discussed. In order to demonstrate the strength of the present methodology in a simple and straightforward fashion, the structure has been modeled for zero-bias operating condition. However, the present methodology can be adapted to optimize bicolor QWIPs with the two wavelengths being individually detected at two distinct applied voltages. Operating parameters such as dark current due to thermionic emission, quantum efficiency, photo-responsivity, etc. may also be included in the optimization methodology. Moreover, the optimization algorithm is not limited to the optimization of absorption structures only. The application of the present method to other intersubband devices such as electron-wave filters and quantum-cascade lasers is discussed in a previous work [15]. Formulation of the optimization algorithm is presented in the next section. In Section III, the design steps of the dual-band (two-color) equal-absorption QWIP structure are presented in detail. Section IV presents the Fourier transform infrared (FTIR) spectroscopic experimental results for the verification of the zero-bias absorption spectrum of the QWIP structure.

II. Theoretical Background

A. Real and Complex Eigenenergies

The initial step in the present method is to find the eigenstates supported by a quantum heterostructure. A quantum structure

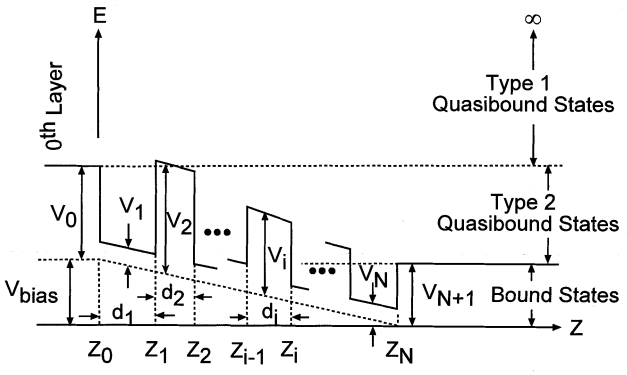

Fig. 1. Schematic representation of a biased semiconductor quantum heterostructure. The energy ranges of bound, type 1 QB, and type 2 QB states are shown.

can support three distinct kinds of eigenstates as identified in Fig. 1. Bound states are associated with electrons confined in both directions by quantum barriers. Type 1 quasibound (QB) states are defined as having classically free propagation through both the left and the right boundaries of the multilayered structure ($Z < 0$ and $Z > L$ in Fig. 1). These states exist at energies that are higher than all conduction band edges and are also referred to as "continuum" or "extended" states. Type 2 QB states have classically free propagation either to the right or to the left of the heterostructure and cannot propagate in the opposite direction due to an infinitely thick barrier. Both types of QB states are analogous to leaky modes in electromagnetic waveguides [16]. QB states may arise, for example, through quantum mechanical constructive interference causing carrier localization. All three types of eigenstates of a given quantum structure are determined under the single-band effective-mass approximation using the argument principle method (APM) in conjunction with the transfer matrix method as described in [17]. The time-independent single-band effective-mass Schroedinger equation for the ith layers of the heterostructure with effective mass m_i^* can be written as

$$\frac{d^2}{dz^2}\psi_i(z)+\frac{2m_i^*}{\hbar^2}\left[E-E_t-V_i-v(z)\right]\psi_i(z)=0,\ \text{for } z_{i-1}\le z\le z_i \tag{1}$$

where $\psi_i(z)$ represents the envelope wavefunction, E is the total electron energy, E_t is the transverse electron energy, V_i is the potential energy in the ith layer, and $v(z)$ is the externally applied potential energy ($v(z) = V_{\text{Bias}}\left[1-(z-z_0)/(z_N-z_0)\right]$ in Fig. 1). The quantity $v(z)$ relates to the applied voltage bias $u(z)$ as $v(z) = -eu(z)$, where e is the magnitude of the electron charge. The transverse energy E_t is assumed to be zero for simplicity. The boundary conditions at the interface of the ith and the $(i-1)$th layer are given by [18] $\psi_i(z_i) = \psi_{i+1}(z_i)$, and $(1/m_i^*)(d/dz)\psi_i(z_i) = (1/m_{i+1}^*)(d/dz)\psi_{i+1}(z_i)$. For the unbiased case $v(z) = 0$ and the wavefunction of each layer is the sum of two complex exponentials representing left- and right-propagating waves $\psi_i(z) = A_i\exp[j\kappa_i(z-z_{i-1})] + B_i\exp[-j\kappa_i(z-z_{i-1})]$, where A_i and B_i are the amplitude coefficients. The quantity κ_i represents the complex wavevector in the ith region and is given by $\kappa_i = \pm\sqrt{2m_i^*(E-V_i)/\hbar^2}$. In the case of

externally applied voltage bias, the envelope functions of the heterostructures are no longer linear combinations of exponentials. An analytical solution of the Schroedinger equation cannot be found for an arbitrary potential. In this case, the region is divided into a finite number of sufficiently small constant-potential steps.

Using the above form for the envelope wavefunctions for successive applications of the boundary conditions allows the amplitude coefficients at the two boundary layers ($i = 0$ and $i = N+1$) to be related by a transfer matrix $\mathcal{M}$. The eigen-energies of the structure are extracted by finding the roots of the complex function $\mathrm{Det}(\mathcal{M}) = 0$, where Det represents the determinant of the matrix. For QB states, "leaky" boundary conditions are imposed on the wavefunctions and a complex transcendental equation is formed. The complex roots of the equation correspond to the QB states of the quantum heterostructure. These roots are calculated via a novel complex arithmetic technique based on the APM [17]. These complex QB energies have the form $\tilde{E} = E_r - jE_i$, where $E_i \geq 0$. The imaginary part of the energy signifies the finite lifetime of the QB state. The total probability of finding the electron inside the structure decreases exponentially in time, with the spatial confinement time given by $\tau_{\mathrm{sc}} = \hbar/2E_i$ [19]. Spatial characteristics of the QB wavefunction include exponentially increasing left and right tails. This is analogous to leaky-mode behavior in slab waveguides and is associated with leakage of electrons out of the structure. On the other hand, bound states decay exponentially outside the structure and therefore have real eigenenergies and infinite lifetimes. The QB states do not have finite wavefunctions at infinity and, therefore, do not satisfy the normal orthogonality conditions of bound states [20]. These nonorthogonal QB states can be considered as superpositions of multiple real energy eigenstates with an energy-dependent dephasing [21].

B. Simulated Annealing (SA) Optimization

The iterative algorithm presented in this paper is a union of the APM described above with SA, a globally convergent optimization technique. SA borrows its name from thermodynamics. After slow cooling or annealing, a metal arrives at its state of lowest energy. SA attempts to minimize a function in a manner similar to annealing to find its global minima. Corana *et al.*'s [22] implementation of SA for continuous variables is used in the present methodology in conjunction with APM. SA explores the target function's entire surface by performing random walks in M parameter space, where M represents the number of optimization variables. A rough view of the parameter space is first obtained by moving with large step lengths. The step lengths in each of the M directions are controlled by a parameter called temperature T. The step length and temperature are coupled so that falling T produces decreasing steps. As the algorithm progresses and T falls, it focuses on the most promising area within the parameter space. SA attempts to optimize the function while moving both uphill and downhill in order to escape local minima. Decisions on uphill movement also contain a random element. For the iterative algorithm presented in this paper, SA was adopted as the optimization algorithm of choice for a variety of reasons. SA is largely independent of the starting values, often a critical input in conventional optimization algorithms such as the maximum likelihood method [23]. SA makes less stringent assumptions about the candidate function than do other algorithms. SA can deal more easily with functions that have ridges and plateaus as compared to the genetic optimization algorithm, which has difficulty with flat parameter spaces [24]. It is also possible to restrict SA optimization to a subset of the parameter space to incorporate fabrication constraints.

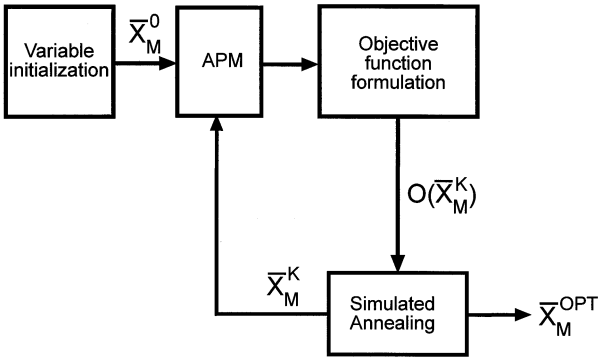

Fig. 2. Flowchart of the iterative optimization algorithm based on APM and SA.

The SA algorithm can be easily transferred to the domain of quantum heterostructure design. The M variables that define the parameter space are device physical parameters, such as individual layer thicknesses d_i, potential barrier heights V_i, number of layers, total device length, applied bias V_{Bias}, etc. A parameter vector $\bar{X}_M = [X_1, \ldots, X_M]^T$ is defined whose entries correspond to the physical parameters (d_i, V_i etc.) to be optimized. An objective function is formulated in order to describe the ideal performance of the heterostructure. The objective function $O(\bar{X}_M)$ is defined in terms of performance variables such as transition energy ΔE_{ij} between states i and j, corresponding dipole matrix elements Z_{ij}, confinement lifetime of eigenstates τ_{sc}, lifetime ratio $R = \tau_i/\tau_j$, etc. These performance variables in turn depend on the physical parameter vector $\bar{X}_M = [X_1, \ldots, X_M]^T$. SA finds in M parameter space the global minima of the objective function thus defined, and determines the physical parameter vector $\bar{X}_M^{OPT}$ which produces a system as close as possible to the ideal. A flow chart of the iterative algorithm is presented in Fig. 2. An informed guess of the physical parameters serves as the initial choice of vector $\bar{X}_M^0$ which initializes the performance parameters by executing APM. Henceforth, SA randomly produces new parameter vectors $\bar{X}_M^K$, where K is the iteration index. Upper and lower bounds on the values of each element of $\bar{X}_M^K$ are incorporated into the algorithm to produce physically realizable results. The randomly produced $\bar{X}_M^K$ is the input to the APM algorithm which determines new performance variables to calculate the objective function $O(\bar{X}_M^K)$. This iterative process is repeated until a predefined convergence criterion is achieved. A nonparabolic effective mass model can also be incorporated within the iterative algorithm as discussed in [15].

III. Bicolor QWIP With Equal Absorption Peaks

A. Initial Design

In order to obtain a bicolor detector, the first step is to define a structure with two spectral ranges of absorption. The two atmospheric windows ($\lambda = 3$–5 μm and $\lambda = 8$–12 μm) are

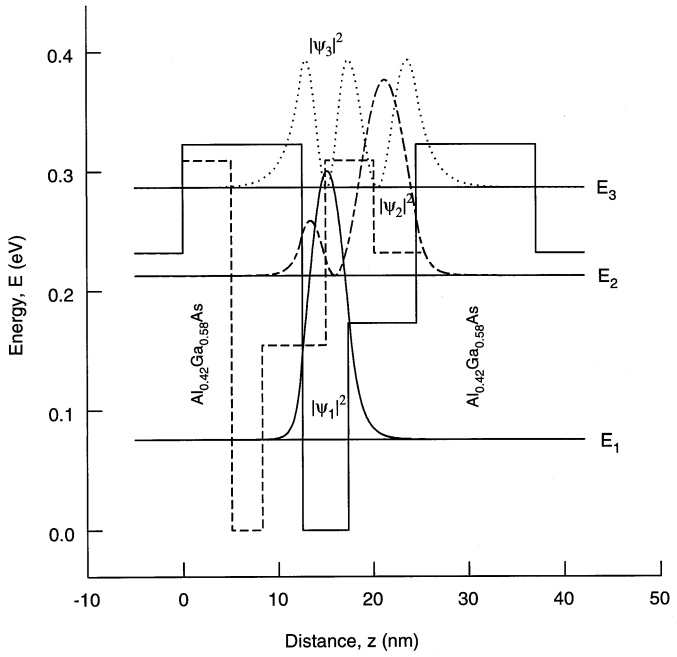

Fig. 3. Optimized design of a bicolor QWIP with equal absorption peaks at λ_{12} and λ_{13}. Squared magnitude of the wavefunctions for first (bound), second (bound), and third (QB) states and corresponding energy levels are shown. The detector is surrounded by $Al_{0.3}Ga_{0.7}As$ input/output regions. The dashed line represents the initial design.

targeted as the two detection bands of interest. A quantum heterostructure with at least three eigenstates is required. The proposed quantum-well detector uses a bound-to-bound and a bound-to-QB transition. Bound-to-bound ($B \leftrightarrow B$) transitions in quantum wells typically exhibit narrow spectral widths, while the bound-to-extended ($B \leftrightarrow E$) transitions are greatly broadened [8]. By the use of a QB ($B \leftrightarrow QB$) excited state, the spectral width of the second transition is made much narrower. The initial design of the bicolor QWIP is shown in Fig. 3 (represented by the dashed line). The input/output regions consist of $Al_{0.3}Ga_{0.7}As$. The detector has four quantum layers: 5.1 nm of $Al_{0.4}Ga_{0.6}As$, 3.2 nm of GaAs, 6.7 nm of $Al_{0.2}Ga_{0.8}As$, and 5.1 nm of $Al_{0.4}Ga_{0.6}As$. The $Al_{0.4}Ga_{0.6}As$ barriers to the left and right of the central asymmetric step quantum well are included to give rise to a strong QB state resonance. The step quantum well is chosen to break the symmetry of the structure. The heterostructure has two bound states and one QB state: $E_1 = 106.88$ meV, $E_2 = 215.85$ meV, and $\tilde{E}_3 = 330.22 - j9.35$ meV. All the eigenstates of the structure have been found via APM as described in Section II. The transition energies are $\Delta E_{12} = 109$ meV and $\Delta E_{13} = 223$ meV. This corresponds to $\lambda_{12} = 11.4$ μm and $\lambda_{13} = 5.56$ μm. Wavelength λ_{13} falls within the MWIR atmospheric window and λ_{12} falls within the LWIR atmospheric window. Of key importance is the dipole matrix element values, $Z_{12} = 1.51$ nm and $Z_{13} = 0.82$ nm, since they define the strength of the corresponding transition. The absorption coefficient α_{ji} for optical transition between states i and j is given by [26]

$$\alpha_{ji} = \frac{2\pi e^2 |Z_{ij}|^2}{n\epsilon_0 \lambda} \times \frac{\frac{\Gamma}{2}}{\left(\frac{\Gamma}{2}\right)^2 + (E_j - E_i - \frac{hc}{\lambda})^2} \times \frac{m^* k_B T}{\pi \hbar^2 L_z} \ln \frac{1 + \exp^{(E_F - E_i)/k_B T}}{1 + \exp^{(E_F - E_j)/k_B T}} \quad (2)$$

where T is the operating temperature, E_F is the Fermi energy, n is the refractive index, e is the magnitude of the electronic charge, and λ is the wavelength of the incident radiation. The linewidth of the Lorentzian Γ in the above equation is approximated as $\Gamma = [(\hbar/\tau_i) + (\hbar/\tau_j) + \Delta E_I]$, where ΔE_I represents homogeneous/inhomogeneous broadening and is assumed to be 20 meV at 77 *K*. The quantities τ_i and τ_j are the lifetimes of eigenstates i and j respectively. The total absorption coefficient in a heterostructure is then calculated by summing the absorption coefficients $\sum_{ij} \alpha_{ji}(\lambda)$ for all possible transitions. The broadening factor Γ for the $B \leftrightarrow B$ transition is determined by ΔE_I only, since the lifetimes (τ_i and τ_j) for both bound states are infinite. However, for the $B \leftrightarrow QB$ transition, the finite lifetime of the QB state must be considered. If the QB state is weakly bound, then the broadening factor $\Gamma_{B \leftrightarrow QB}$ is significantly larger than $\Gamma_{B \leftrightarrow B}$. Consequently, the values of the absorption coefficients at peak detection wavelengths $\alpha_{P(B \leftrightarrow QB)}$ and $\alpha_{P(B \leftrightarrow B)}$ are unequal. The goal of the present optimization problem is to make the ratio R of the two peak values, $\alpha_{P(3 \leftrightarrow 1)}$ and $\alpha_{P(2 \leftrightarrow 1)}$ as close to unity as possible. For the initial configuration, this ratio is $R = 0.3$.

B. Parameter Identification, Fabrication Constraints, and Optimization

The initial configuration of the bicolor QWIP structure has four quantum layers. Ideally, all the individual layer thicknesses, aluminum compositions, and the input/output composition may be chosen as independent optimization parameters. However, the molecular beam epitaxy (MBE) machine used for the sample growth has only two aluminum cells. Therefore, only two independent aluminum compositions are possible for the bicolor QWIP structure. A third aluminum composition is also possible, with the constraint

$$x_c = \frac{1 - x_a x_b}{(1 - x_a)(1 - x_b)} \quad (3)$$

where x_a and x_b are the two independent aluminum compositions. With these constraints in mind, five parameters ($M = 5$) are identified for the optimization process of the bicolor QWIP. The input/output region aluminum composition (x_0) is left unchanged at 30%. This leaves only one more aluminum composition that may be varied independently for the optimization process. The aluminum composition of the second layer is chosen to be zero (GaAs well). The aluminum composition of the third layer is varied as an independent parameter ($x_I = x_3$). The composition of the first and fourth layers are set to be equal ($x_1 = x_4$) and is determined according to (3). All the individual layer thicknesses are varied independently and $\bar{X}_M = [x_I, d_1, d_2, d_3, d_4]^T$. The aluminum composition of the individual layers is constrained by $0 \leq x_i \leq 0.45$ in order to retain direct bandgap operation. The individual layer thickness d_i has a lower bound of eight monolayers for feasibility of fabrication, and an upper bound of 60 monolayers in order to retain electron coherence. Only two bound states are allowed for the heterostructure. In addition, only one QB state is allowed within the energy range 232–340 meV. The absence of additional states ensures unambiguous transitions. The objective of the optimization process is to make the ratio of the two absorption peaks $\alpha_{P(31)}/\alpha_{P(21)}$ as close to unity as possible

without reducing the values of the dipole matrix elements Z_{12} and Z_{13}. These transition wavelengths are constrained to fall within the range $\lambda_{12} = 8$–$12\ \mu$m ($B \leftrightarrow B$) and $\lambda_{13} = 4$–$6\ \mu$m ($B \leftrightarrow QB$). These values of the detection wavelengths fall within the two atmospheric windows with λ_{12} in the LWIR range and λ_{13} in the MWIR range. The objective function to be minimized $O(\bar{X}_M)$ is defined as follows:

$$
\begin{aligned}
&O(\bar{X}_M) \\
&= A + B + C + D + E + F + G / \text{ where} \\
A &= \begin{cases} 0, & \text{if } |\Delta E_{12} - 130| \le 25 \text{ meV} \\ 10|\Delta E_{12}(\bar{X}_M) - 130|, & \text{otherwise} \end{cases} \\
B &= \begin{cases} 0, & \text{if } |\Delta E_{13} - 250| \le 40 \text{ meV} \\ 10|\Delta E_{13}(\bar{X}_M) - 250|, & \text{otherwise} \end{cases} \\
C &= 50\,000 \times \left(1 - \frac{\alpha_{P(31)}(\bar{X}_M)}{\alpha_{P(21)}(\bar{X}_M)}\right) \\
D &= \begin{cases} \frac{1000}{(Z_{12}(\bar{X}_M) - 0.5)}, & \text{if } Z_{12} \ge 1.51 \text{ nm} \\ 1000|Z_{12}(\bar{X}_M) - 1.51|, & \text{otherwise} \end{cases} \\
E &= \begin{cases} \frac{1000}{(1 + (Z_{13}(\bar{X}_M) - 0.82))}, & \text{if } Z_{13} \ge 0.82 \text{ nm} \\ 1000|Z_{13}(\bar{X}_M) - 0.82|, & \text{otherwise} \end{cases} \\
F &= \begin{cases} 0, & \text{if } \tau_3 \ge 200 \text{ fs} \\ 30000 \times (200 - \tau_3(\bar{X}_M)), & \text{otherwise} \end{cases} \\
G &= \begin{cases} 0, & \text{if } x_1(\bar{X}_M) \le 0.45 \\ 1000 \times (x_1(\bar{X}_M) - 0.45), & \text{otherwise} \end{cases} . \qquad (4)
\end{aligned}
$$

Here, all energies are expressed in millielectronvolts, dipole matrix elements in nanometers, and lifetimes in femtoseconds. The weights in (4) are found empirically after a few runs of the algorithm to determine the dynamics of the objective function in each one of the M parameters. Terms A and B ensure the appropriate transition wavelengths λ_{12} and λ_{13}, and are set to the minimum value of zero once ΔE_{ij} falls within the desired range. C ensures the equality of the two absorption peaks. Terms D and E are added to make the dipole matrix elements larger than the original values of 1.51 and 0.82 nm if possible. Term F sets a lower limit on the lifetime of the QB state in order to prevent a very weak resonance. As can be seen, C is emphasized more than the other terms in the cost function since the goal of the algorithm is to make the ratio of the absorption peaks unity. F is given the second highest emphasis in order to find a very strongly localized QB state. Otherwise, the algorithm was found to converge on structures that possessed QB states with very small lifetimes. The term G is added to ensure that the aluminum composition of the first and the second layers ($x_1 = x_4$), derived from constant x_0 and randomly chosen x_2 do not exceed 0.45. A method to force stable solutions is included in the algorithm by introducing random perturbations at each iteration in the vector $\bar{X}_M^K$. Each time the SA algorithm produces a new $\bar{X}_M^K$, each of its elements x_2, d_1, d_2, d_3, d_4 are perturbed l times, producing l different $\bar{X}_M^K$ vectors. The APM is executed l times (within each iteration loop) to formulate l different sets of functional parameters (Z_{12}, Z_{13}, ΔE_{13} etc.) in order to produce l different objective functions. The average of these intermediate objective functions is taken to formulate $O(\bar{X}_M^K)$. For this particular optimization problem, $l = 4$ is used. This perturbation method ensures that the optimization algorithm does not reach a sharp minima in the parameter space so that random fluctuations in the fabrication process do not degrade the device performance. The optimized bicolor QWIP is shown in Fig. 3. As desired, the structure possesses two bound states and one QB state with the correct energy spacings to yield $\lambda_{12} = 9.1\ \mu$m and $\lambda_{13} = 5.9\ \mu$m. The eigenstate values are $E_1 = 75.92$ meV, $E_2 = 212.88$ meV, and $E_3 = 286.58 - j0.02$ meV. The QB state is a very strongly localized one. The dipole matrix elements $Z_{12} = 1.34$ nm and $Z_{13} = 1.07$ nm. The ratio $R = \alpha_{P(31)}/\alpha_{P(21)} = 0.99$ and the detector has equal absorption peaks at both detection wavelengths. The modulus square of the eigen-wavefunctions are shown in Fig. 3 (solid line). The dashed curve corresponds to the potential profile of the original design. However, the algorithm calculates the individual layer aluminum compositions and layer thicknesses to the 16th significant figures. These values are rounded off for fabrication feasibility. The aluminum compositions are rounded off to the second significant figures and the layer thicknesses are rounded off to the nearest 0.1 nm. The effect of conduction band nonparabolicity is included in the calculation following [25]. After these adjustments, the ratio $R = \alpha_{P(31)}/\alpha_{P(21)} = 0.93$.

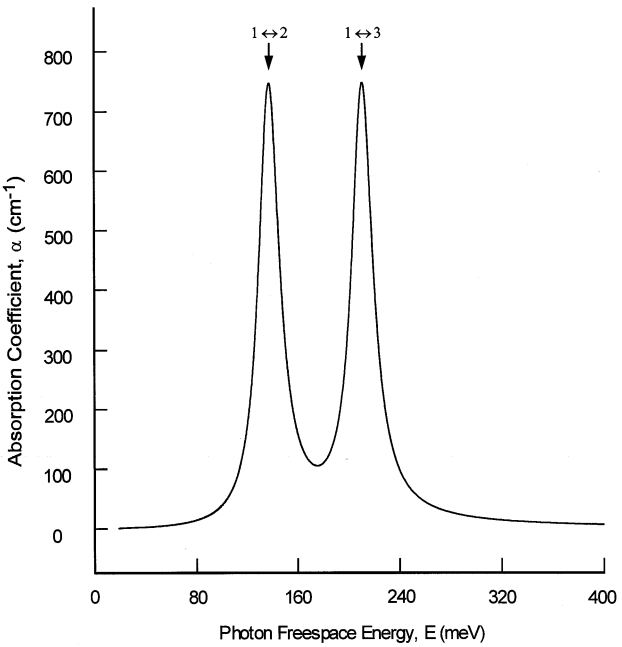

Fig. 4. Absorption coefficient of the bicolor equal-absorption-peak QWIP as a function of free-space photon energy at 77 K.

C. Fermi Level and Charge Distribution

Three possible optical transitions exist in the bicolor equal-absorption-peak QWIP described above. However, only the 1↔2 and the 1↔3 transitions must be observed. Therefore, the structure must be doped such that only the lowest subband E_1 is populated, and the 2↔3 transition is not observed due to lack of electron population in the second subband. With this in mind, the central part of the GaAs well in the QWIP structure is doped at $1.0 \times 10^{18}/\text{cm}^3$. Assuming complete ionization of donors, the Fermi energy is calculated from the charge neutrality condition $N_D^+ = \sum_i N_i$, where N_D^+ is the ionized donor sheet-density and N_i is the two-dimensional subband population [27]. For the present calculation, complete

TABLE I
EQUAL-ABSORPTION-PEAK QWIP STRUCTURE SPECIFICATION

Layer No.	Layer Name	*Al* Comp.	Thickness (nm)	Doping
1	1st barrier	0.4177	12.5	0
2	1st well	0.00	4.8	$1.0 \times 10^{18} cm^{-3}$, central 4.0 nm
3	2nd well	0.224	7.2	0.0
4	2nd barrier	0.4177	12.5	0.0
5	spacer	0.70	70.0	0.0
Total thickness = 107.0 nm				

ionization is assumed and $N_D^+ = N_D = N_1 + N_2 + N_3$. The subband population of the ith eigenstate is given by

$$N_i = \frac{m^* k_B T}{\pi \hbar^2} \ln\left[1 + \exp^{(E_F - E_i)/k_B T}\right] \tag{5}$$

where E_i is the eigenenergy, E_F is the Fermi energy, and m^* is the effective mass of electrons in GaAs [28]. Assuming an operating temperature of 77 K for the bicolor QWIP structure, E_F is found to be 89.4 meV. For this value of the Fermi energy, only the lowest subband of the bicolor QWIP is populated as desired, and the population difference ΔN_{31} is equal to the population difference ΔN_{21}. Using this value of Fermi energy, the total absorption coefficient $\alpha = \sum_{ij} \alpha_{ji}$ is calculated for the optimized bicolor equal-absorption-peak QWIP structure and is shown in Fig. 4 as a function of free-space photon energy.

The doping profile is chosen in order to balance the electron distribution of the lowest bound state (the only occupied state of the bicolor QWIP) so that "flatband" conduction band profile is retained under zero bias. Only the central 4.0 nm of the GaAs well is doped and the flat-band condition is retained within $\approx$ 0.5 meV. Therefore, the space-charge effect on the potential profile can be neglected and no self-consistent calculation is necessary. Free-carrier absorption in doped semiconductors must be taken into account in intersubband device design. For the doping level used in the bicolor QWIP, the free-carrier absorption increases as the third power of the wavelength [29]. The free-carrier absorption coefficient values (at $\lambda_{12} = 9.05\ \mu$m and $\lambda_{13} = 5.89\ \mu$m) are calculated to be more than ten times less than the corresponding intersubband peak absorbance values. Therefore, the induced intersubband absorbance spectrum of the optimized bicolor QWIP is easily verifiable through the FTIR measurement.

D. Sample Geometry and Epitaxial Layer Specification

The previous sections discuss the heterostructure design of the bicolor equal-absorption-peak QWIP. For practical devices, this basic heterostructure must be repeated a few times, separated by a spacer layer, in order to have significant infrared signal absorption. For the bicolor QWIP, the total heterostructure thickness $L_{\text{device}} = 37$ nm. The thickness of the spacer layer $L_{\text{spacer}} = 70$ nm so that there is no coupling between the wavefunctions of different devices. Table I shows the specification of the QWIP/spacer unit. The number of repetitions of the QWIP/spacer unit is chosen to be 50. This active layer is grown on top of a semi-insulating (100) oriented *GaAs* substrate followed by an undoped $Al_{0.3}Ga_{0.7}As$ buffer layer. The active layer is capped with undoped GaAs. The thicknesses of the buffer and the cap layers must be chosen carefully according to the experimental geometry. The absorption characteristics of the equal-absorption-peak QWIP were measured using a Bruker IFS/66 Fourier transform infrared (FTIR) spectrometer incorporating a five-times beam condenser to focus light onto a polished end of the sample. The sample geometry is shown in Fig. 5. Only the polarization component of incident radiation normal to the growth direction contributes to intersubband absorption in the absence of strain [30]. Thus, in order to increase the net absorption, a multipass geometry is used by polishing the ends of the sample at $\theta_P = 17°$. There are multiple advantages of using a shallow wedge angle of 17°. The polished edge of the sample presents a large area and this facilitates sample/beam alignment. In addition, a beam propagating parallel to planes of the two dimensional epitaxial layers would be incident on the wedge at Brewster's angle ($\theta_B = 73°$) with respect to the surface normal. As such, the TM polarized incident radiation is completely transmitted into the sample without being reflected. The transmitted beam traverses the sample length in a zig-zag geometry as shown in Fig. 5, and absorption within the active layer is enhanced. At the GaAs/air interface, the infrared beam goes through total internal reflection and the incident and the reflected beams interfere with each other. The intensity of the interference pattern is given by $I(z) = 2[1 + \cos(2k_0 n_0 z \sin\theta'/2)]$, where k_0 is the free-space wave vector, n_0 is the refractive index of the material, and θ' is the angle between the two interfering beams and for the proposed geometry $\theta'/2 = 90° - \theta = 56°$ (Fig. 5). The electric field in the growth direction goes to zero at the surface, and the length of the cap layer should be chosen so that the quantum-well active layer is not placed at the null of the intensity pattern. To complicate matters, there are two infrared wavelengths of interest. Following the design methodology of [31], the active layer is placed at a distance of 0.53 μm from the top GaAs/air interface to maximize the absorption for both infrared wavelengths of interest. Thus, the thickness of the upper cap layer is chosen to be 0.53 μm. The buffer layer also has the same thickness. Table II shows the complete wafer specifications.

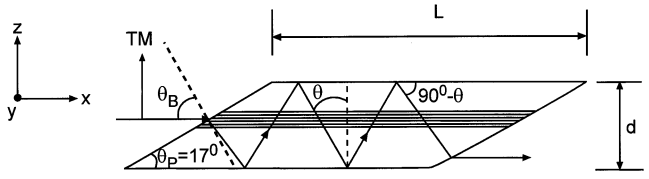

Fig. 5. Experimental geometry for the verification of the absorption spectrum of the optimized bicolor QWIP.

TABLE II
WAFER SPECIFICATION

Layer Name	*Al* Comp.	Thickness (μm)	Doping
upper cap layer	0.0	0.53	0.0
active layer	see Table 1	5.385	see Table 1
buffer layer	0.3	0.53	0.0
semi-insulating substrate	0.0	500.0	0.0

IV. EXPERIMENTAL VERIFICATION OF BICOLOR EQUAL-ABSORPTION-PEAK QWIP STRUCTURE SPECTRUM

The semiconductor wafer was cleaved into a 10 mm $\times$ 5 mm piece using a CarlSuss 100 Wafer Cleaver. The next step in sample preparation is polishing the small cleaved piece at a 17° facet. A specialized polishing chuck was made for this purpose using Molybdenum. Molybdenum was used in order to protect the polishing chuck from corrosive polishing fluid. The sample is initially lapped at an angle on a 3-μm-grit polishing paper using 3 μm grit aluminum–hydroxide polishing powder slurry. Fine polishing of the facet is done by polishing the sample on a special polishing cloth (Chemcloth by Logitech) using a sodium–hypochlorite based solution (Chemlox by Logitech). As the final step, the sample is chemically cleaned using acetone, methanol, DI water, and is blown dry using dry nitrogen gas. The backside of the sample is also polished in order to reduce scattering during infrared signal transmission. The sample is cleaved from the central portion of the wafer in order to ensure growth uniformity over the dimensions of the cleaved piece. A liquid N_2 temperature mercury cadmium telluride (MCT) detector is used for the intersubband absorption experiment. The FTIR scans are obtained at 300 K. The absorption spectrum is presented in Fig. 6.

The QWIP absorption spectrum exhibits two main peaks at 1560 cm^{-1} and 1082 cm^{-1}. These two peaks correspond to the $1 \rightarrow 3$ and $1 \rightarrow 2$ intersubband absorptions. There is a much smaller peak at 767cm^{-1} which is a phonon absorption as described in [29]. The corresponding transition energy values are $\Delta E_{12} = 134$ meV and $\Delta E_{13} = 193.4$ meV. The theoretical values are $\Delta E_{12} = 136$ meV and $\Delta E_{13} = 204$ meV. The $1 \rightarrow 2$ transition energy deviates by only 2 meV from theoretical prediction. Therefore, it is assumed that the first and second eigenstate positions correspond almost exactly to the theoretical values ($E_1 = 75.92$ meV and $E_2 = 212.88$ meV). The small discrepancy between the theoretical and the experimental values of ΔE_{13} can be contributed solely to the third eigenstate position. The $1 \rightarrow 3$ transition energy deviates by 11 meV from theoretical prediction. This corresponds to a 3.9% deviation from theory and is well within acceptable limits. The APM over-estimates the QB eigenstates by a few percent due to the nonorthogonal nature of these states [15]. In addition, there is an energy lowering associated with the energy peaks at higher temperatures. The conduction band nonparabolicity coefficient is temperature dependent [29]. Since nonparabolicity affects the higher energy levels, the lowering of the transition energy is pronounced for the $1 \rightarrow 3$ transition involving the third eigenstate. In addition to the temperature-dependent nonparabolicity effect, many-body effects, such as the electron–electron exchange interaction [32] and depolarization effects [33], are also responsible for temperature-dependent energy peak shifts. Therefore, at the design temperature of 77 K, the transition energy ΔE_{13} would be closer to the theoretical value of 204 meV. At 77 K, only the first eigenstate is populated and the $2 \rightarrow 3$ transition does not occur. The electric dipole matrix value Z_{23} is relatively large and is close to 3 nm. At 300 K, the second eigenstate is only slightly populated ($N_1 = 99.4\%$ $N_2 = 0.6\%$) and the $2 \rightarrow 3$ transition should exist. It is not possible to observe this transition due to a very strong phonon absorption band around 550 cm^{-1}. However, due to the scarcity of electrons in the second eigenstate, the $2 \rightarrow 3$ transition is very weak even at room temperature, and does not effect the overall spectrum significantly. The absorption peaks at 1560 cm^{-1} and 1082 cm^{-1} disappear for TE-polarized infrared radiation, thus confirming that these peaks are indeed intersubband absorptions. Other than the phonon resonance, no other peak which could be confused with an intersubband resonance is observed in the sample. It is worth mentioning that the only manipulation performed on the spectrum of Fig. 6 is a very small baseline correction in order to facilitate data analysis. The low noise level and the clarity of the spectrum are extraordinarily good. The absorption peaks are remarkable in their sharpness and Lorentzian lineshapes. For the doping level of the bicolor QWIP, the free-carrier absorption increases as λ^3 and degrades signal integrity in the long wavelength regime. The lack of long wavelength free-carrier absorption tail of the bicolor QWIP spectrum validates the design efforts expended in minimizing this unwanted feature.

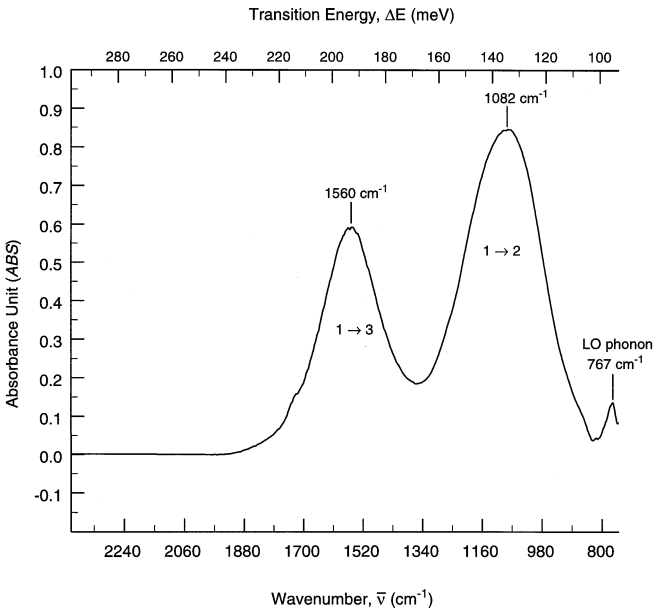

Fig. 6. Absorption spectrum of the bicolor equal-absorption-peak QWIP as a function of free-space photon wavenumber and energy at 300 K. The intersubband absorption peak for the $1 \rightarrow 3$ transition occurs at $\bar{\nu} = 1560$ cm^{-1} ($\Delta E_{13} = 193.4$ meV and $\lambda_{13} = 6.4$ μm). The intersubband absorption peak for the $1 \rightarrow 2$ transition occurs at $\bar{\nu} = 1082$ cm^{-1} ($\Delta E_{12} = 134$ meV and $\lambda_{12} = 9.24$ μm). The LO phonon absorption peak occurs at $\bar{\nu} = 767$ cm^{-1} ($\Delta E_{LO} = 95$ meV and $\lambda_{LO} = 13$ μm).

The next experimental data of interest are the linewidths of the intersubband transitions. The linewidth of the peaks are measured by performing a Lorentzian linefit to the experimental data. The linewidth values are $\Gamma_{21} = 33$ meV and $\Gamma_{31} =$

27 meV. The thermal energy of the electrons at room temperature is $k_BT = 26$ meV and this value accounts for almost all of the linewidth broadening for the intersubband transitions. The lifetimes of the excited states can be deduced from the relation $\tau_{ji} = \hbar/\Gamma_{ji}$. The lifetimes $\tau_{21} = 0.02$ ps and $\tau_{31} = 0.024$ ps. Since the third state is a QB state, its spectrum has a finite linewidth given by $FWHM = \hbar/2E_i$, where E_i is the imaginary part of the complex eigenenergy $\tilde{E}_3$. The FWHM of the third state is very narrow with a value of 0.04 meV. Using the relation $\Gamma = [(\hbar/\tau_i) + (\hbar/\tau_j) + (\hbar/\tau_{\rm sc}) + \Delta E_I]$, the intersubband electron-phonon scattering time $\tau_{\rm sc}$ can be found. The electron-LO phonon scattering time from the third to the first state $\tau_{\rm sc31} = 0.69$ ps. The value of $\tau_{\rm sc21} = 0.09$ ps. These values fall in the range of previously published results [34]. The electron–phonon scattering rate from the second to the first state is higher than the scattering rate from the third to the first state. The large electric dipole matrix element Z_{12} is directly proportional to higher electron-phonon scattering rate [34]. In addition, the room-temperature measurement increases the scattering rate since the electron-LO phonon scattering is strongly dependent on temperature. It has been demonstrated that for any given wavelength of an intersubband device, increasing the temperature from 77 K to 300 K increases the electron–phonon scattering rate by almost an order of magnitude [35]. The intersubband experimental data exhibits minimum signs of interface or impurity scattering. This fact verifies the good quality of the heterostructure interfaces. If the heterostructure interfaces are sufficiently rough then scattering could destroy the absorption effects either by increased lifetime broadening, or by lack of conservation of transverse momentum wavevector. In addition, electrons can be trapped by deep energy states at poor quality interfaces and refrain from participating in intersubband transitions.

The intersubband oscillator strengths/dipole matrix element values can be deduced from the experimental data by integrating the areas under the Lorentzian curves that fit the experimental peaks. This area, or the integrated absorption fraction (IAF), is related to the intersubband oscillator strength f_{mn} as [36]

$$IAF = \frac{e^2 h f_{mn}}{4\epsilon_0 c n m^*} \frac{(N_{sm} - N_{sn}) N_B N \sin^2(\theta)}{\cos(\theta)}. \qquad (6)$$

Here, $\theta = 34^\circ$ for the geometry of Fig. 5, ϵ_0 is the free-space permittivity, c is the speed of light in vacuum, h is the Planck's constant, and N_{sm} is the sheet electron density of the mth eigenstate. The experimental IAFs are found to be $IAF_{12} \approx 43$ meV and $IAF_{13} \approx 25$ meV. Using (6), the electric dipole matrix elements are deduced to be $Z_{12} = 1.35$ nm and $Z_{12} = 0.83$ nm. The experimental value of Z_{12} is in excellent agreement with the theoretical prediction of $Z_{12} = 1.34$ nm. However, the experimental Z_{13} varies from the theoretical value of $Z_{13} = 1.07$ nm by $\approx 20\%$. There is an uncertainty associated with electric dipole matrix elements involving QB states due to the nonorthogonal nature of these states [15]. The uncertainty associated with Z_{13} is found to be $\pm 4\%$, as calculated following the numerical model presented in Section II. It is difficult to predict the exact nature of the deviation from theoretical prediction. The pronounced temperature-dependent shift of the $1 \rightarrow 3$ transition will also modify the electric dipole matrix element by changing the overlap between the wavefunctions. The ratio of the peak intensities at λ_{13} and λ_{12} is experimentally found to be 0.71. The theoretical prediction of the ratio $R = \alpha_{P31}/\alpha_{P21}$ is approximated to be 0.86 at room temperature. This discrepancy can be accounted for by the fact that the third eigenstate energy value and the electric dipole matrix element Z_{12} are overestimated by 10 meV and 0.23 nm. The oscillator strength for transition between states i and j is proportional to $\Delta E_{ij}|Z_{ij}|^2$. The deviation in ΔE_{13} and Z_{13} can reduce the value of R to 77% from a theoretical prediction of 86%. In addition, it has been demonstrated in [31] that random fluctuations in device parameters such as aluminum compositions and layer thicknesses can cause a deviation of up to 5% in the value of R, thus reducing it to 73%. The experimentally calculated value of 71% is close to this value of 73%. It must be noted that there are uncertainties associated with quantum heterostructure simulation on more fundamental levels. The analogy between a real quantum well and a theoretical two-dimensional system has limitations. There are also uncertainties associated with the envelope function boundary conditions at heterostructure interfaces, the true value of electron density, the degree of ionization of the donors, the Fermi energy, the true well widths, and the true barrier heights. In view of these uncertainties, the agreement between theory and experiment is very good. In the context of a multicolor QWIP manipulating transitions within the same heterostructure, the ratio of the absorption peak heights ($R = 0.71$ at 300 K) as designed and demonstrated in this paper is the highest ratio achieved to this date. The closest value reported in the literature is $R = 0.3$, as reported by Martinet *et al.* [11].

V. Summary

In summary, an iterative algorithm for the optimized design of QWIPs was presented and verified. This methodology is not limited to QWIPs and can be applied equally well to other intersubband devices such as quantum cascade lasers, electron-energy filters etc. This technique is a globally convergent algorithm with no restriction on the number of parameters to be optimized. The algorithm also incorporates an efficient tool for determining all the eigenstates of a heterostructure. The versatility of the present method is demonstrated by the optimized synthesis of an equal-absorption-peak QWIP structure. The zero-bias absorption spectrum of the optimized QWIP structure is verified with FTIR measurements. This method, which relies on the APM or eigenstate determination, and on SA for parameter optimization, meets all the criteria for a robust, globally convergent optimization algorithm for QWIPs.

References

[1] A. Rogalski and K. Jozwikowski, "*GaAs/AlGaAs* quantum well infrared photoconductors versus HgCdTe photodiodes for long-wavelength infrared applications," *Optical Eng.*, vol. 33, pp. 1477–1488, May 1994.

[2] B. F. Levine, C. G. Bethea, G. Hasnain, V. O. Shen, E. Pelve, R. R. Abbott, and S. J. Hsieh, "High sensitivity low dark current 10 μm GaAs quantum well infrared photodetectors," *Appl. Phys. Lett.*, vol. 56, pp. 851–853, Feb. 1990.

[3] D. D. Coon and R. P. G. Karunasiri, "New mode of IR detection using quantum wells," *Appl. Phys. Lett.*, vol. 34, pp. 649–651, Aug. 1995.

[4] K. K. Choi, *The Physics of Quantum Well Infrared Photodetectors.* Singapore: World Scientific, 1997.

[5] K. K. Choi, M. Z. Tidrow, M. Taysing-Lara, W. H. Chang, C. H. Kuan, C. W. Farley, and F. Chang, "Low dark current infrared hot-electron transistor for 77 K operation," *Appl. Phys. Lett.*, vol. 63, pp. 908–910, Aug. 1993.

[6] S. D. Gunapala, S. V. Bandara, A. Singh, J. K. Liu, B. Rafol, E. M. Luong, J. M. Mumolo, N. Q. Tran, D. Z. -Y. Ting, J. D. Vincent, C. A. Shott, J. Long, and P. D. LeVan, "640 × 486 long-wavelength two-color GaAs/AlGaAs quantum well infrared photodetector (QWIP) focal plane array camera," *IEEE Trans. Electron Devices*, vol. 47, pp. 963–971, May 2000.

[7] A. G. Steel, H. C. Liu, M. Buchanan, and Z. R. Wasilewski, "Importance of the upper state position in the performance of quantum well intersubband infrared detectors," *Appl. Phys. Lett.*, vol. 59, pp. 3625–3627, Dec. 1991.

[8] S. V. Bandara, S. D. Gunapala, J. K. Liu, E. M. Luong, J. M. Mumolo, W. Hong, D. K. Sengupta, and M. J. McKelvey, "10 – 16 μm broadband quantum well infrared photodetector," *Appl. Phys. Lett.*, vol. 72, pp. 2427–2429, May 1998.

[9] I. Grave, A. Shakouri, N. Kuze, and A. Yariv, "Voltage-controlled tunable GaAs/AlGaAs multistack quantum well infrared detector," *Appl. Phys. Lett.*, vol. 60, pp. 2362–2364, May 1992.

[10] K. Kheng, M. Ramsteiner, H. Schneider, J. D. Ralson, F. Fuchs, and P. Koidl, "Two-color GaAs/(AlGaAs) quantum well infrared detector with voltage-tunable spectral sensitivity at 3 – 5 and 8 – 12 μm," *Appl. Phys Lett.*, vol. 61, pp. 666–668, Aug. 1992.

[11] E. Martinet, E. Rosencher, F. Luc, P. Bois, E. Costard, and S. Delaitre, "Switchable bicolor (5.5 – 9.0 μm) infrared detector using asymmetric GaAs/AlGaAs multiquantum well," *Appl. Phys. Lett.*, vol. 61, pp. 246–248, July 1992.

[12] M. Z. Tidrow, K. K. Choi, C. W. Farley, and F. Chang, "Multicolor infrared detection using a voltage tunable bandpass filter," *Appl. Phys. Lett.*, vol. 65, pp. 2996–2998, Dec. 1994.

[13] J. C. Chiang and S. S. Li, "A two stack indirect-barrier/triple-coupled quantum well infrared detector for mid-wavelength and long–wavelength infrared dual band detection," *Appl. Phys. Lett.*, vol. 71, pp. 3546–3548, Dec. 1997.

[14] H. C. Liu, P. H. Wilson, M. Lamm, A. G. Steele, Z. R. Wasilewski, J. Li, M. Buchanan, and J. G. Simmons, "Low dark current dual band infrared photodetector using thin AlAs barriers and $\Gamma - X$ mixed intersubband transition in *GaAs* quantum wells," *Appl. Phys. Lett.*, vol. 64, pp. 475–477, Jan. 1994.

[15] N. Imam, E. N. Glytsis, and T. K. Gaylord, "Semiconductor intersubband laser/detector performance optimization using a simulated annealing algorithm," *Superlatt. Microstruct.*, vol. 30, pp. 29–43, July 2001.

[16] T. Tamir and F. Y. Kou, "Varieties of leaky waves and their excitation along multilayered structures," *IEEE J. Quantum Electron.*, vol. QE-22, pp. 544–551, Apr. 1986.

[17] E. Anemogiannis, E. N. Glytsis, and T. K. Gaylord, "Bound and quasibound state calculation for biased/unbiased semiconductor quantum heterostructure," *IEEE J. Quantum Electron.*, vol. 29, pp. 2731–2740, Nov. 1993.

[18] G. Bastard, "Superlattice band structure in the envelope-function approximation," *Phys. Rev.*, vol. B24, pp. 5693–5697, Nov. 1981.

[19] P. J. Price, "Resonant tunneling properties of heterostructures," *Superlatt. Microstruct.*, vol. 2, pp. 593–596, Aug. 1986.

[20] R. E. Collin, *Field Theory of Guided Waves*. New York: IEEE Press, 1991.

[21] L. D. Landau and E. M. Lifshitz, *Quantum Mechanics, Non-Relativistic Theory*. London, U.K.: Pergamon, 1958.

[22] A. Corana, M. Marchesi, C. Martini, and S. Ridella, "Minimizing multimodal functions of continuous variables with the simulated annealing algorithm," *ACM. Trans. Math. Soft.*, vol. 13, pp. 262–280, Sept. 1987.

[23] J. S. Cramer, *Econometric Application of Maximum Likelihood Methods*. New York: Cambridge Univ. Press, 1986.

[24] D. E. Goldberg, *Genetic Algorithms in Search, Optimization, and Machine Learning*. Reading, MA: Addison-Wesley, 1989.

[25] D. F. Nelson, R. C. Miller, and D. A. Kleinman, "Band nonparabolicity effects in semiconductor quantum wells," *Phys. Rev.*, vol. B35, pp. 7770–7773, May 1987.

[26] S. L. Chuang, *Physics of Optoelectronic Devices*. New York: Wiley, 1995.

[27] G. N. Henderson, L. C. West, T. K. Gaylord, C. W. Roberts, E. N. Glytsis, and M. T. Asom, "Optical transition to above-barrier quasibound states in asymmetric semiconductor heterostructures," *Appl. Phys. Lett.*, vol. 62, pp. 1432–1434, Mar. 1993.

[28] N. Imam, E. N. Glytsis, and T. K. Gaylord, "Spatially varying effective mass effects on energy level populations in semiconductor quantum devices," Superlatt. Microstruct., vol. 32, 2002, submitted for publication.

[29] J. S. Blakemore, "Semiconducting and other major properties of GaAs," *J. Appl. Phys.*, vol. 53, pp. R123–R181, Oct. 1982.

[30] E. Rosencher, B. Vinter, and B. F. Levine, Eds., *Intersubband Transitions in Quantum Wells*. New York: Plenum, 1992, vol. 288, NATO ASI Series, Series B, Physics.

[31] N. Imam, "Analysis, Design, and Testing of Semiconductor Intersubband Devices," Ph.D. dissertation, Georgia Inst. Technol., Atlanta, 2002.

[32] M. O. Manasreh, "Origin of the blueshift in the intersubband absorption in $GaAs/Al_{0.3}Ga_{0.4}As$ multiple quantum wells," *Phys. Rev.*, vol. B43, pp. 9996–9999, Aug. 1991.

[33] M. O. Manasreh, F. Szmulowicz, D. A. Fischer, K. R. Evans, and C. E. Stutz, "Intersubband infrared absorption in $GaAs/Al_{0.3}Ga_{0.4}As$ quantum well structure," *Appl. Phys. Lett.*, vol. 57, pp. 1790–1792, Oct. 1990.

[34] R. Ferrier and G. Bastard, "Evaluation of some scattering times for electrons in unbiased and biased single and multiple quantum well structures," *Phys. Rev.*, vol. B40, pp. 1074–1086, July 1989.

[35] N. E. I. Etteh and P. Harrison, "Carrier scattering approach to the origins of dark current in mid-and far-infrared (terahertz) quantum-well intersubband photodetectors (QWIP's)," *IEEE. J. Quantum Electron.*, vol. 37, pp. 672–675, May 2001.

[36] L. C. West and S. J. Eglash, "First observation of an extremely large-dipole infrared transition within the conduction band of a GaAs quantum well," *Appl. Phys. Lett.*, vol. 46, pp. 1156–1168, June 1985.

Neena Imam received the B.S. degree in electrical engineering from California Institute of Technology, Pasadena, in 1993, the M.S. degree in electrical engineering from Case Western Reserve University, Cleveland, OH, in 1995, and the Ph.D. degree in electrical engineering from Georgia Institute of Technology, Atlanta, in 2002. Her Master's thesis involved the design and simulation of acousto-optic tunable filter (AOTF)-based optical networks and fabrication of $LiNbO_3$ based AOTFs. Her doctoral research involved the analysis, design, and testing of semiconductor intersubband devices.

She is currently with the Computer Science and Mathematics Division of Oak Ridge National Laboratory, Oak Ridge, TN.

Dr. Imam is a member of Phi Beta Kappa and Eta Kappa Nu.

Elias N. Glytsis (S'87–M'88–SM'91) received the B.S. degree from the National Technical University of Athens, Athens, Greece, in 1982 and the M. S. and Ph.D. degrees from Georgia Institute of Technology, Atlanta, in 1984 and 1987, respectively.

He joined the faculty of the School of Electrical and Computer Engineering, Georgia Institute of Technology, Atlanta, as an Assistant Professor in 1988, and since 2000, has been a Professor. His current research interests are in electromagnetic theory of holographic and diffractive grating couplers, diffractive optical interconnections, fiber grating devices, optoelectronic devices, semiconductor quantum electron wave devices and applications, intersubband emitters and detectors, design-optimization-integration software, and electromagnetic problems in power systems. He has published over 95 journal publications and over 80 conference papers and holds eight U.S. patents. He has been co-guest editor of two special issues of the *Optical Society of America* on grating diffraction. He has been a Topical Editor of the *Journal of Optical Society of America A* on scattering and grating diffraction between 1992–1997. He has also been a guest editor of the *Microelectronics Journal* for a special issue on quasibound states in quantum heterostructure devices.

Dr. Glytsis is a Fellow of the Optical Society of America, and a member of LEOS and the Greek Society of Professional Engineers.

Thomas K. Gaylord (S'65–M'70–SM'77–F'83) received the B.S. degree in physics and the M.S. degree in electrical engineering from the University of Missouri–Rolla and the Ph.D. degree in electrical engineering from Rice University, Houston, TX.

He is with Georgia Institute of Technology, Atlanta, where he is Julius Brown Chair and Regents' Professor of Electrical and Computer Engineering. He is the author of some 350 technical publications and 25 patents in the areas of diffractive optics, optoelectronics, and semiconductor devices.

Dr. Gaylord received the "Curtis W. McGraw Research Award" from the American Society for Engineering Education; the IEEE Centennial Medal, the IEEE Graduate Teaching Award, the Georgia Tech Outstanding Teacher Award, and the "Engineer of the Year Award" from the Georgia Society of Professional Engineers. He is a Fellow of the Optical Society of America and of the American Association for the Advancement of Science.

Kwong-Kit Choi (M'00–SM'00) received the Ph. D. degree in physics from Yale University, New Haven, CT, in 1984.

He is a co-inventor of the quantum-well infrared photodetector (QWIP). Subsequently, he made many inventions that further advanced the technology. His inventions include the infrared hot-electron transistor, the voltage-tunable multicolor QWIP, the corrugated-QWIP, and the quantum grid infrared photodetector. Collaborated with Goddard Space Flight Center, he has demonstrated a 1024×1024 QWIP camera, which is peaked at 8.7 μm, and also demonstrated thermal imaging at a very long wavelength of 16.2 μm. Other technical contributions include the invention of four spectroscopy techniques for device and material characterization and the invention of quantum collector transistors for high-speed digital applications. He also made significant contributions in fundamental solid-state physics in the area of electron localization, many-body interaction, quantum Hall effects, and material defects. He has authored and co-authored 80 refereed journal articles, four book chapters, and one book *The Physics of Quantum Well Infrared Photodetectors* (Singapore: World Scientific, 1997). He has been awarded ten patents, with two pending. He is an Army Research Laboratory (ARL) Senior Research Scientist (ST).

Dr. Choi is a Felow of ARL and of the American Physical Society, and a member of SPIE. He was inducted into NASA Space Technology Hall of Fame in year 2001.

Peter G. Newman received the B.A. degree in biology from the University of California, San Diego, in 1978.

He has been performing molecular-beam epitaxy (MBE) rowth for nearly 25 years, the last 14 with the U.S. Army Research Laboratory in Adelphi, Maryland. He was previously with the University of Southern California, Los Angeles, and Rockwell International Science Center, Thousand Oaks, CA. His accomplishments include growth of the first HBTs and QWIPs by MBE, as catalogued in over 110 publications to date.

Lisa Detter-Hoskin was born in Mechanicsburg, PA, in 1960. She received the B.A. degree in chemistry in from Susquehanna University, Selinsgrove, PA, in 1982, the Ph.D. degree in inorganic chemistry from Purdue University, West Lafayette, IN, in 1987, and the M.S. degree in management of technology from Southern Polytechnic Institute, Marietta, GA, in 1996.

In 1992, she joined the Georgia Tech Research Institute (GTRI) Materials Analysis Center (MAC), Atlanta, GA, where she works on method development and evaluation of numerous materials using infrared spectroscopy, electron microscopy, X-ray diffraction, and thermal and surface analysis techniques. Her specialty includes structural elucidation, corrosion, and failure mechanistic studies of metals and polymers. Since 1995, she has served as the MAC group leader.

Dr. Detter-Hoskin is a member of the American Chemical Society and the American Microbeam Analysis Society.